Available online at www.sciencedirect.com
SCIENCE DIRECT®
Journal of Computational Physics 210 (2005) 519–534
JOURNAL OF COMPUTATIONAL PHYSICS
www.elsevier.com/locate/jcp

A deterministic solver for the transport of the AlGaN/GaN 2D electron gas including hot-phonon and degeneracy effects

M. Galler, F. Schürrer *

Institute of Theoretical and Computational Physics, Graz University of Technology, Petersgasse 16, A-8010 Graz, Austria

Received 6 December 2004; received in revised form 24 April 2005; accepted 27 April 2005
Available online 11 July 2005

Abstract

The transport of the two-dimensional electron gas formed at an AlGaN/GaN heterostructure in the presence of strain polarization fields is investigated. For this purpose, we develop a deterministic multigroup model to the Boltzmann transport equations. The envelope wave functions for the confined electrons are calculated using a self-consistent Poisson–Schrödinger solver. The electron gas degeneracy and hot phonons are included in our transport equations. Numerical results are given for the dependence of macroscopic quantities on the electric field strength and on time and for the electron and phonon distribution functions. We compare our results to those of Monte Carlo simulations and with experiments.

PACS: 73.61.Ey; 73.50.Fq; 73.50.Bk

Keywords: 2DEG; AlGaN/GaN heterostructure; Multigroup model; Hot phonon effects

1. Introduction

The application of GaN and related nitride semiconductors is of great interest in the fabrication of modern semiconductor devices, since these materials demonstrate an essential radiation hardness and operate at high voltages and high temperatures [1]. In addition, nitride heterostructures feature the formation of high-mobility two-dimensional electron gas (2DEG) channels due to their strong spontaneous and piezoelectric polarization. The sheet electron density can exceed $10^{13}\,\mathrm{cm}^{-2}$ without intentional doping, especially at AlGaN/GaN heterojunctions. Hence, the high electron density combined with high operational voltages makes AlGaN/GaN channels attractive for high-power/high-frequency applications.

* Corresponding author. Tel.: +43 316 873 8177; fax: +43 316 873 8677.
E-mail addresses: galler@itp.tu-graz.ac.at (M. Galler), schuerrer@itp.tu-graz.ac.at (F. Schürrer).

0021-9991/$ - see front matter
doi:10.1016/j.jcp.2005.04.021

In this paper, we propose multigroup model equations for directly solving the transport equations, which govern the particle distribution at an AlGaN/GaN heterojunction. As shown recently [2], the longitudinal optical (LO) phonon controlled energy dissipation and hot phonon effects as well as the degeneracy of the 2DEG play an important role for the particle transport in such structures. Therefore, the kinetic equations, on which our multigroup model is based, are the two-dimensional Bloch–Boltzmann–Peierls (BBP) equations for electrons and polar optical phonons [3,4]. The quantitative comparisons of simulations and experiments can only be satisfying, when the physics of the considered problem is regarded in detail. Hence, the potential confining the electrons at the heterojunction is assembled in our simulations as the self-consistent solution to the Poisson–Schrödinger system, fully based on material data for GaN and AlGaN.

So far, mainly Monte Carlo techniques have been used for investigating the carrier transport in heterostructure channels. However, the treatment of such problems by means of deterministic approaches constitutes an interesting alternative to the usual procedure, since these methods provide noise-free results and high efficiency when studying transient regimes, as it has been shown for the particle transport in polar semiconductors [5,6]. To our knowledge, the application of deterministic solution techniques to the BBP equations for the investigation of hot-phonon effects and degeneracy phenomena at AlGaN/GaN heterojunctions has not been performed yet.

Our paper is organized as follows: Section 2 describes the physical model on which our calculations are based. In Section 3, we present the 2D-BBP equations and summarize the transition rates, which are applied for modeling the electron–phonon interactions. In Section 4, we introduce the multigroup model equations used for investigating the transport of the 2DEG at an AlGaN/GaN heterostructure. Finally, Section 5 deals with our numerical results. We present the self-consistent solution of the Poisson–Schrödinger system for the confining potential at the AlGaN/GaN heterojunction as well as the stationary-state values and the transients of macroscopic quantities in comparison to Monte Carlo calculations and experiments. Additionally, distribution functions for both the electrons and the LO phonons are displayed.

2. The physical model

We consider the transport of a 2DEG formed at a wurtzite, Ga-face AlGaN/GaN heterojunction consisting of a 25 nm $Al_{0.15}Ga_{0.85}N$ undoped layer and a thick undoped GaN layer. The c-axis of the wurtzite lattice is assumed to be perpendicular to the AlGaN/GaN interface. This allows us to describe the quantum states of the electrons at the interface with one transverse effective mass m^* and one set of energy subbands with the energy eigenvalues ε_ν and the normalized envelope wave functions φ_ν. In contrast to the confined electrons, we treat the phonons as three-dimensional particles. This is reasonable because of the small changes in the mechanical parameters at the AlGaN/GaN heterojunction. In Fig. 1, we display the geometry used in our considerations. The z-axis is chosen normal to the AlGaN/GaN interface at $z = 0$. Hence, electrons are confined in z-direction and move semiclassically free in the (x,y) plane parallel to the heterojunction. This homogeneous transport is driven by an electric field $\mathbf{E}_\parallel = (\mathscr{E}_x, 0, 0)$ in x-direction. We include scattering mechanisms for the electrons caused by acoustic and longitudinal optical phonons in our transport model. Scattering by ionized impurities is neglected since we deal with an undoped heterojunction, where the 2DEG is induced only by spontaneous and piezoelectric polarization charges. In the considered range of the electric field strength, electron scattering into upper valleys is supposed to be negligible. Thus, we employ a one-valley multi-subband spherical, parabolic model band structure. Electron real space transfer and sharing effects are neglected in our calculations.

The electron energy $E^\nu(\mathbf{k}_\parallel)$ in the νth energy subband and the electron wave vector $\mathbf{k}_\parallel$ are related by the spherical, parabolic energy momentum rule [3]

$$E^\nu(\mathbf{k}_\parallel) = \frac{\hbar^2 k_\parallel^2}{2m^*} + \varepsilon_\nu, \tag{1}$$

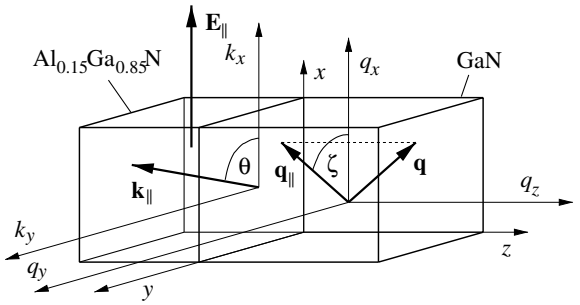

Fig. 1. Schematic illustration of the AlGaN/GaN heterojunction including the chosen coordinate systems for space and wave vectors of electrons and phonons.

with $k_\parallel = |\mathbf{k}_\parallel|$. This implies that the modulus of the electron wave vector $k_\parallel^\nu$ in the subband ν is determined by $k_\parallel^\nu(E) = [2m^*(E-\varepsilon_\nu)]^{1/2}\Theta(E-\varepsilon_\nu)/\hbar$ with the Heaviside function Θ for the given energy E. The energy of longitudinal optical (LO) phonons $\hbar\omega_{\mathrm{LO}}$ is connected with the phonon wave vector $\mathbf{q}$ according to the Einstein approximations $\hbar\omega_{\mathrm{LO}}(\mathbf{q}) = \hbar\omega_{\mathrm{LO}}$ [7].

3. 2D Bloch–Boltzmann–Peierls equations and 2D transition rates

The electron system is described by a set of one-particle distributions functions $f^\nu(\mathbf{k}_\parallel,t)$, which gives the probability to find an electron in the infinitesimal volume $\mathrm{d}^2k_\parallel$ around $\mathbf{k}_\parallel$ at time t in the νth subband. The evolution equation for $f^\nu(\mathbf{k}_\parallel,t)$ is the 2D electron Bloch–Boltzmann–Peierls equation. Expressing $\mathbf{k}_\parallel$ in polar coordinates $\mathbf{k}_\parallel^\nu = (k_\parallel^\nu(E)\cos\theta, k_\parallel^\nu(E)\sin\theta)$ with the polar angle θ between $\mathbf{k}_\parallel$ and $\mathbf{E}_\parallel$ (cp. Fig. 1) and introducing the new unknown function $F^\nu(E,\theta,t) = Z_{\mathrm{el}}^\nu(E)f^\nu(E,\theta,t)$ with the electron density of states $Z_{\mathrm{el}}^\nu(E) = m^*\Theta(E-\varepsilon_\nu)/4\pi^2\hbar^2$, we obtain the energy dependent formulation of the 2D electron BBP equation. It reads

$$\partial_t F^\nu + \partial_E\left[a_1^\nu(E,\theta)F^\nu\right] + \partial_\theta\left[a_2^\nu(E,\theta)F^\nu\right] = \mathscr{C}_1[F^\nu] + \mathscr{C}_2[F^\nu], \tag{2}$$

with

$$a_1^\nu(E,\theta) = -\frac{e\mathscr{E}_x}{m^*}\hbar k_\parallel^\nu(E)\cos\theta, \quad a_2^\nu(E,\theta) = \frac{e\mathscr{E}_x}{\hbar k_\parallel^\nu(E)}\sin\theta. \tag{3}$$

In this equation, two types of scattering mechanisms are included. The collision term

$$\begin{aligned}\mathscr{C}_1[F^\nu] = \sum_\mu \int_0^\infty \mathrm{d}E' \int_0^{2\pi} \mathrm{d}\theta' \{ & c_1(\mathbf{k}_\parallel^\nu - \mathbf{k}_\parallel^{\mu'})F^\mu(\mathbf{k}_\parallel^{\mu'})[Z_{\mathrm{el}}^\nu(E) - F^\nu(\mathbf{k}_\parallel^\nu)]g(\mathbf{k}_\parallel^\nu - \mathbf{k}_\parallel^{\mu'})\delta(E'-E+\hbar\omega_{\mathrm{LO}}) \\ & + c_1(\mathbf{k}_\parallel^{\mu'} - \mathbf{k}_\parallel^\nu)F^\mu(\mathbf{k}_\parallel^{\mu'})[Z_{\mathrm{el}}^\nu(E) - F^\nu(\mathbf{k}_\parallel^\nu)][g(\mathbf{k}_\parallel^{\mu'} - \mathbf{k}_\parallel^\nu)+1]\delta(E'-E-\hbar\omega_{\mathrm{LO}}) \\ & - c_1(\mathbf{k}_\parallel^{\mu'} - \mathbf{k}_\parallel^\nu)F^\nu(\mathbf{k}_\parallel^\nu)[Z_{\mathrm{el}}^\mu(E') - F^\mu(\mathbf{k}_\parallel^{\mu'})]g(\mathbf{k}_\parallel^{\mu'} - \mathbf{k}_\parallel^\nu)\delta(E'-E-\hbar\omega_{\mathrm{LO}}) \\ & - c_1(\mathbf{k}_\parallel^\nu - \mathbf{k}_\parallel^{\mu'})F^\nu(\mathbf{k}_\parallel^\nu)[Z_{\mathrm{el}}^\mu(E') - F^\mu(\mathbf{k}_\parallel^{\mu'})][g(\mathbf{k}_\parallel^\nu - \mathbf{k}_\parallel^{\mu'})+1]\delta(E'-E+\hbar\omega_{\mathrm{LO}})\},\end{aligned} \tag{4}$$

with the scattering function c_1 depending on the interaction mechanism and $\mathbf{k}_\parallel^\nu = \mathbf{k}_\parallel^\nu(E,\theta)$, $\mathbf{k}_\parallel^{\mu'} = \mathbf{k}_\parallel^\mu(E',\theta')$ couples the electron-LO phonon system. On the other hand, $\mathscr{C}_2[F^\nu]$ refers to an elastic scattering mechanism with the scattering function c_2,

$$\begin{aligned}\mathscr{C}_2[F^\nu] = \sum_\mu \int_0^\infty \mathrm{d}E' \int_0^{2\pi} \mathrm{d}\theta' \{ & c_2(\mathbf{k}_\parallel^{\mu'}, \mathbf{k}_\parallel^\nu)F^\mu(\mathbf{k}_\parallel^{\mu'})[Z_{\mathrm{el}}^\nu(E) - F^\nu(\mathbf{k}_\parallel^\nu)] \\ & - c_2(\mathbf{k}_\parallel^\nu, \mathbf{k}_\parallel^{\mu'})F^\nu(\mathbf{k}_\parallel^\nu)[Z_{\mathrm{el}}^\mu(E') - F^\mu(\mathbf{k}_\parallel^{\mu'})]\}\delta(E'-E),\end{aligned} \tag{5}$$

where $\mathbf{k}_\parallel^\nu = \mathbf{k}_\parallel^\nu(E,\theta)$ and $\mathbf{k}_\parallel^{\mu'} = \mathbf{k}_\parallel^\mu(E',\theta')$.

Similarly as for electrons, we represent the wave vector $\mathbf{q}$ of LO phonons in cylindrical coordinates $\mathbf{q} = (q_\parallel \cos\zeta, q_\parallel \sin\zeta, q_z)$, where $q_\parallel$ is the modulus of $\mathbf{q}_\parallel$, i.e., the projection of $\mathbf{q}$ onto the $(x$–$y)$ plane, and ζ is the polar angle between $\mathbf{q}_\parallel$ and $\mathbf{E}_\parallel$ as illustrated in Fig. 1. Here, we introduce the 2D LO phonon distribution $g(\mathbf{q}_\parallel,t)$, which is obtained from the 3D distribution function by averaging it with respect to q_z. The dynamics of LO phonons is governed by a phonon BBP equation similar to that of the electrons. Defining $G(q,\zeta,t) = Z_{\mathrm{LO}}(q_\parallel)g(q,\zeta,t)$ with the LO phonon density of states $Z_{\mathrm{LO}}(q_\parallel) = q_\parallel/4\pi^2$ leads to

$$\partial_t G = \mathscr{D}_1[G] + \mathscr{D}_2[G]. \tag{6}$$

Electron–phonon interaction is described by the collision term

$$\begin{aligned}\mathscr{D}_1[G] = \sum_{\nu,\mu} \int_0^\infty \mathrm{d}E \int_0^{2\pi} \mathrm{d}\theta \{ & c_1(\mathbf{k}_\parallel^\nu, \mathbf{k}_\parallel^\nu - \mathbf{q}_\parallel) F^\nu(\mathbf{k}_\parallel^\nu)[1 - f^\mu(\mathbf{k}_\parallel^\nu - \mathbf{q}_\parallel)][G(\mathbf{q}_\parallel) + Z_{\mathrm{LO}}(q_\parallel)]\delta(E' - E + \hbar\omega_{\mathrm{LO}}) \\ & - c_1(\mathbf{k}_\parallel^\nu, \mathbf{k}_\parallel^\mu + \mathbf{q}_\parallel) F^\nu(\mathbf{k}_\parallel^\nu)[1 - f^\mu(\mathbf{k}_\parallel^\nu + \mathbf{q}_\parallel)][G(\mathbf{q}_\parallel)]\delta(E' - E - \hbar\omega_{\mathrm{LO}})\}. \end{aligned} \tag{7}$$

The phonon–phonon interaction term $\mathscr{D}_2$ is considered according to the relaxation time approximation

$$\mathscr{D}_2[G] = -\frac{1}{\tau_{\mathrm{LO}}}[G(\mathbf{q}_\parallel) - Z_{\mathrm{LO}}(q_\parallel) g_{\mathrm{BE}}], \tag{8}$$

with the Bose–Einstein distribution $g_{\mathrm{BE}} = [\exp(\hbar\omega_{\mathrm{LO}}/k_{\mathrm{B}}T_{\mathrm{L}}) - 1]^{-1}$ and the relaxation time τ_{LO}.

Concerning the transition rates for electron–phonon interactions, we apply the following. The electrons interact with acoustic phonons through the deformation potential and the electrostatic polarization associated with atomic vibrations. In wurtzite structures, the deformation potential in the central valley is a diagonal second-rank tensor D. The value of D_{zz} is in general different from $D_{xx} = D_{yy}$. However, experimental data are not available for these quantities. Therefore, we assume equal diagonal elements and treat the deformation potential tensor as a scalar quantity [8]. This implies that the scattering function $c_{2,\mathrm{ADP}}$ for acoustic deformation potential scattering reads in the elastic approximation as

$$c_{2,\mathrm{ADP}}(\mathbf{k}_\parallel^\nu, \mathbf{k}_\parallel^{\mu\prime}) = \frac{2\pi D_{\mathrm{A}}^2 k_{\mathrm{B}} T_{\mathrm{L}}}{\hbar\rho v_{\mathrm{s}}^2} \frac{1}{W_{\mu\nu}}, \tag{9}$$

with $v_{\mathrm{s}} = (v_{\mathrm{l}} v_{\mathrm{t}}^2)^{1/3}$ and

$$\frac{1}{W_{\mu\nu}} = \int_{-\infty}^{\infty} \mathrm{d}z |\varphi_\mu(z)|^2 |\varphi_\nu(z)|^2. \tag{10}$$

The strength of the piezoelectric scattering is determined by the dimensionless electromechanical coupling coefficient K^2, which contains contributions of both the longitudinal (LA) and the transverse (TA) acoustic phonons. Following [9], we obtain

$$K^2 = \frac{\langle e_{\mathrm{LA}}^2 \rangle}{\kappa_{\mathrm{st}} \varepsilon_0 c_{\mathrm{LA}}} + \frac{\langle e_{\mathrm{TA}}^2 \rangle}{\kappa_{\mathrm{st}} \varepsilon_0 c_{\mathrm{TA}}}, \tag{11}$$

where c_{LA} and c_{TA} are the angular averages of the elastic constants describing the propagation of LA and TA waves and

$$\langle e_{\mathrm{LA}}^2 \rangle = \frac{1}{105}[8(2e_{15} + e_{31})^2 + 12(2e_{15} + e_{31})e_{33} + 15e_{33}^2], \tag{12a}$$

$$\langle e_{\mathrm{TA}}^2 \rangle = \frac{1}{105}[6(e_{33} - e_{15} - e_{31})^2 + 16(e_{33} - e_{15} - e_{31})e_{15} + 48e_{15}^2]. \tag{12b}$$

This implies that the scattering function $c_{2,\mathrm{PZ}}$ for screened piezoelectric scattering reads

$$c_{2,\mathrm{PZ}}(\mathbf{k}_\parallel^{\nu}, \mathbf{k}_\parallel^{\mu\prime}) = \frac{2\pi k_\mathrm{B} T_\mathrm{L} e^2}{\hbar \kappa_\mathrm{st} \varepsilon_0} \frac{K^2}{W_{\mu\nu}} \left[\frac{\delta_{\mu\nu}}{\left(|\mathbf{k}_\parallel^{\mu\prime} - \mathbf{k}_\parallel^{\nu}| + q_\mathrm{s}\right)^2} + \frac{1-\delta_{\mu\nu}}{|\mathbf{k}_\parallel^{\mu\prime} - \mathbf{k}_\parallel^{\nu}|^2} \right], \tag{13}$$

with the screening parameter,

$$q_\mathrm{s} = \sum_{\nu} \frac{m^* e^2}{2\pi \kappa_\mathrm{st} \varepsilon_0 \hbar^2} f^{\nu}(0), \tag{14}$$

derived from the matrix-random phase approximation [10].

Electron-LO phonon coupling in wurtzite crystals is different from the well-known cubic case. The electrons interact with both the longitudinal optical (LO) and the transverse optical (TO) modes rather than with a single LO mode as in cubic lattices. However, it has been shown that the scattering rate for TO scattering is more than two orders of magnitude smaller than that for LO scattering. Moreover, the LO scattering rate in the cubic approximation is valid regardless of the chosen point in the Brillouin zone [11]. Hence, we use the cubic approximation and the formulation of Price [12] for the transition rates, leading to the scattering function $c_{1,\mathrm{POP}}$ for screened polar optical scattering

$$c_{1,\mathrm{POP}(q_\parallel)} = \frac{e^2 \omega_0}{2\varepsilon_0} \left(\frac{1}{\kappa_\mathrm{hf}} - \frac{1}{\kappa_\mathrm{st}} \right) \left[\frac{\pi \delta_{\mu\nu} q_\parallel^2}{(q_\parallel + \pi W_{\mu\nu} q_\parallel^2)(q_\parallel + q_s)^2} + \frac{\pi(1-\delta_{\mu\nu})(\alpha_{\mu\nu} - \beta_{\mu\nu} q_\parallel)}{q_\parallel + \pi W_{\mu\nu}(\alpha_{\mu\nu} - \beta_{\mu\nu} q_\parallel) q_\parallel^2} \right], \tag{15}$$

with

$$\begin{pmatrix} \alpha_{\mu\nu} \\ \beta_{\mu\nu} \end{pmatrix} = \int_{-\infty}^{\infty} \mathrm{d}z \int_{-\infty}^{\infty} \mathrm{d}z' \begin{pmatrix} 1 \\ |z - z'| \end{pmatrix} \varphi_\nu^*(z') \varphi_\mu^*(z') \varphi_\nu(z) \varphi_\mu(z). \tag{16}$$

4. Multigroup model equations

For formulating multigroup equations to the 2D-BBP equations (2) and (6), we introduce the discretization of the independent variables E, θ, $q_\parallel$ and ζ according to

$$E_{i+1/2} = \varepsilon_1 + i\Delta E, \quad i = 0, 1, \ldots, N, \quad \Delta E = \frac{\hbar \omega_\mathrm{LO}}{n_\mathrm{mul}}, \quad n_\mathrm{mul} \in \mathbb{N}, \tag{17a}$$

$$E_i = \varepsilon_1 + \left[i - \frac{1}{2} \right] \Delta E, \quad i = 1, 2, \ldots, N, \tag{17b}$$

$$\theta_{j+1/2} = j\Delta\theta, \quad j = 0, 1, \ldots, M, \quad \Delta\theta = \frac{2\pi}{M}, \tag{17c}$$

$$\theta_j = \left[j - \frac{1}{2} \right] \Delta\theta, \quad j = 1, 2, \ldots, M, \tag{17d}$$

$$q_{x+1/2} = j\Delta q, \quad x = 0, 1, \ldots, R, \quad \Delta q = \frac{q_\mathrm{max}}{R}, \tag{17e}$$

$$\zeta_{y+1/2} = y\Delta\zeta, \quad y = 0, 1, \ldots, S, \quad \Delta\zeta = \frac{2\pi}{S}. \tag{17f}$$

Here, $E_\mathrm{max} = N\Delta E$ and q_max must be chosen in a way that $F^{\nu}(E_\mathrm{max})$ is negligible for all ν, θ and t and $G(q_\mathrm{max})$ is undisturbed by the electron–phonon interaction for all ζ and t. The distribution functions of electrons and phonons are approximated as the finite sums

$$Z^{\nu}_{\mathrm{el}}(E)f^{\nu}(E,\theta,t) = \sum_{i=1}^{N}\sum_{j=1}^{M} n^{\nu}_{ij}(t)\delta(E-E_i)\delta(\theta-\theta_j), \tag{18a}$$

$$Z^{\nu}_{\mathrm{el}}(E)[1-f^{\nu}(E,\theta,t)] = \sum_{i=1}^{N}\sum_{j=1}^{M}[1^{\nu}_{ij}-n^{\nu}_{ij}(t)]\lambda^{\mathrm{E}}_{i}(E)\delta(\theta-\theta_j), \tag{18b}$$

$$Z_{\mathrm{ph}}(q_{\parallel})g(q_{\parallel},\zeta,t) = \sum_{x=1}^{R}\sum_{y=1}^{S} r_{xy}(t)\lambda^{\mathrm{q}}_{x}(q_{\parallel})\lambda^{\zeta}_{y}(\zeta), \tag{18c}$$

$$Z_{\mathrm{ph}}(q_{\parallel})[g(q_{\parallel},\zeta,t)+1] = \sum_{x=1}^{R}\sum_{y=1}^{S}[r_{xy}(t)+1^{\mathrm{p}}_{xy}]\lambda^{\mathrm{q}}_{x}(q_{\parallel})\lambda^{\zeta}_{y}(\zeta), \tag{18d}$$

with $N\times M$ coefficients n^{ν}_{ij} for each electron subband and $R\times S$ phonon coefficients r_{xy}. We remark that $n^{\nu}_{ij}=0$ for $E_i<\varepsilon_{\nu}$ for all θ and t. In ansatz (18), we use

$$\lambda^{\mathrm{E}}_{i}(E) = \begin{cases} \Delta E^{-1}, & \text{if } E\in[E_{i-1/2},E_{i+1/2}],\\ 0, & \text{if } E\notin[E_{i-1/2},E_{i+1/2}], \end{cases} \tag{19}$$

and corresponding expressions for $\lambda^{\mathrm{q}}_{i}(q_{\parallel})$ and $\lambda^{\zeta}_{i}(\zeta)$. Additionally, we apply

$$1^{\nu}_{ij} = \frac{m^*}{4\pi^2\hbar^2}[\Theta(E_{i+1/2}-\varepsilon_{\nu})E_{i+1/2}-\Theta(E_{i-1/2}-\varepsilon_{\nu})E_{i-1/2}]\Delta\theta, \tag{20a}$$

$$1^{\mathrm{p}}_{xy} = \frac{1}{8\pi^2}[q^2_{x+1/2}-q^2_{x-1/2}]\Delta\zeta. \tag{20b}$$

Forming moments of (18) reveals that the macroscopic quantities electron density $\langle n^{\nu}\rangle$, drift velocity $\langle v^{\nu}\rangle$ in direction of the electric field and mean energy $\langle E^{\nu}\rangle$ in the νth subband as well as the phonon density $\langle n^{\mathrm{p}}\rangle$ are simply given by

$$\langle n^{\nu}(t)\rangle = 2\sum_{i=1}^{N}\sum_{j=1}^{M} n^{\nu}_{ij}(t), \tag{21a}$$

$$\langle v^{\nu}(t)\rangle = \frac{2\hbar}{m^*\langle n^{\nu}(t)\rangle}\sum_{i=1}^{N}\sum_{j=1}^{M} k^{\nu}_{\parallel}(E_i)\cos\theta_j n^{\nu}_{ij}(t), \tag{21b}$$

$$\langle E^{\nu}(t)\rangle = \frac{2}{\langle n^{\nu}(t)\rangle}\sum_{i=1}^{N}\sum_{j=1}^{M} E_i n^{\nu}_{ij}(t), \tag{21c}$$

$$\langle n^{\mathrm{p}}(t)\rangle = \sum_{x=1}^{R}\sum_{y=1}^{S} r_{xy}(t). \tag{21d}$$

The evolution equations for the coefficients n^{ν}_{ij} and r_{xy} are obtained by inserting (18) into the 2D-BBP equations (2) and (6) and integrating the result over the cells $C_{ij}=[E_{i-1/2},E_{i+1/2}]\times[\theta_{j-1/2},\theta_{j+1/2}]$ and $D_{xy}=[q_{x-1/2},q_{x+1/2}]\times[\zeta_{y-1/2},\zeta_{y+1/2}]$, respectively. This procedure yields

$$\begin{aligned} &\frac{\partial n^{\nu}_{ij}}{\partial t} + a^{\nu}_1(E_{i+1/2},\theta_j)[n^{\mathrm{E},\nu}_{ij}]^{+} - a^{\nu}_1(E_{i-1/2},\theta_j)[n^{\mathrm{E},\nu}_{ij}]^{-} + a^{\nu}_2(E_i,\theta_{j+1/2})[n^{\theta,\nu}_{ij}]^{+} - a^{\nu}_2(E_i,\theta_{i-1/2})[n^{\theta,\nu}_{ij}]^{-}\\ &\quad = \mathscr{C}_1[n^{\nu}_{ij}] + \mathscr{C}_2[n^{\nu}_{ij}],\\ &\frac{\partial r_{xy}}{\partial t} = 2\mathscr{D}_1[r_{xy}] + \mathscr{D}_2[r_{xy}], \end{aligned} \tag{22}$$

when applying an upwind scheme with linear approximations for the fluxes at the boundaries of C_{ij} with

$$[n_{ij}^{\mathrm{E},v}]^{+} = \begin{cases} n_{ij}^{v} + \frac{s_{ij}^{\mathrm{E},v}}{2}, & \text{if } a_1^v(E_i,\theta_j) > 0, \\ n_{i+1,j}^{v} - \frac{s_{i+1,j}^{\mathrm{E},v}}{2}, & \text{if } a_1^v(E_i,\theta_j) < 0, \end{cases} \tag{23a}$$

$$[n_{ij}^{\mathrm{E},v}]^{-} = \begin{cases} n_{ij}^{v} - \frac{s_{ij}^{\mathrm{E},v}}{2}, & \text{if } a_1^v(E_i,\theta_j) < 0, \\ n_{i-1,j}^{v} + \frac{s_{i-1,j}^{\mathrm{E},v}}{2}, & \text{if } a_1^v(E_i,\theta_j) > 0, \end{cases} \tag{23b}$$

and $s_{ij}^{\mathrm{E},v} = \mathrm{MM}(n_{i+1,j}^{v} - n_{ij}^{v}, n_{ij}^{v} - n_{i-1,j}^{v})$. The MinMod slope limiter [13] is defined by

$$\mathrm{MM}(a,b) = \begin{cases} 0, & \text{if } ab < 0, \\ \max(a,b), & \text{if } a < 0, \\ \min(a,b), & \text{if } a > 0. \end{cases} \tag{24}$$

Similar expressions are used for determining $[n_{ij}^{\theta,v}]^{+}$ and $[n_{ij}^{\theta,v}]^{-}$.

The electron collision terms $C_1[n_{ij}^{v}]$ and $C_2[n_{ij}^{v}]$ read

$$\begin{aligned} \mathscr{C}_1[n_{ij}^{v}] = \sum_{\mu}\sum_{x=1}^{R}\sum_{y=1}^{S}\sum_{a=1}^{N}\sum_{b=1}^{M}\{ & \langle S_{ab\to ij,xy}^{\mu\to v}\rangle^{+} n_{ab}^{\mu}[1_{ij}^{v} - n_{ij}^{v}]r_{xy} + \langle S_{ab\to ij,xy}^{\mu\to v}\rangle^{-} n_{ab}^{\mu}[1_{ij}^{v} - n_{ij}^{v}][r_{xy} + 1_{xy}^{\mathrm{p}}] \\ & - \langle S_{ij\to ab,xy}^{v\to\mu}\rangle^{+} n_{ij}^{v}[1_{ab}^{\mu} - n_{ab}^{\mu}]r_{xy} - \langle S_{ij\to ab,xy}^{v\to\mu}\rangle^{-} n_{ij}^{v}[1_{ab}^{\mu} - n_{ab}^{\mu}][r_{xy} + 1_{xy}^{\mathrm{p}}]\}, \end{aligned} \tag{25a}$$

$$\mathscr{C}_2[n_{ij}^{v}] = \sum_{\mu}\sum_{a=1}^{N}\sum_{b=1}^{M}\{\langle C_{ab\to ij}^{\mu\to v}\rangle n_{ab}^{\mu}[1_{ij}^{v} - n_{ij}^{v}] - \langle C_{ij\to ab}^{v\to\mu}\rangle n_{ij}^{v}[1_{ab}^{\mu} - n_{ab}^{\mu}]\}, \tag{25b}$$

with the collision coefficients

$$\begin{aligned} \langle S_{ij\to ab,xy}^{v\to\mu}\rangle^{\pm} = \int_{C_{ij}} \mathrm{d}E\,\mathrm{d}\theta \int_{C_{ab}} \mathrm{d}E'\,\mathrm{d}\theta' \frac{c_1[\pm(\mathbf{k}_{\parallel}^{\mu\prime} - \mathbf{k}_{\parallel}^{v})]}{Z_{\mathrm{LO}}(|\mathbf{k}_{\parallel}^{\mu\prime} - \mathbf{k}_{\parallel}^{v}|)} \delta(E - E_i)\lambda_a^{\mathrm{E}}(E')\delta(\theta - \theta_j)\delta(\theta' - \theta_b)\lambda_x^{\mathrm{q}}(|\mathbf{k}_{\parallel}^{\mu\prime} - \mathbf{k}_{\parallel}^{v}|) \\ \times \lambda_y^{\zeta}(\pm\mathrm{acos}|\mathbf{k}_{\parallel}^{\mu\prime} - \mathbf{k}_{\parallel}^{v}|^{-1})\mathbf{e}_x \cdot (\mathbf{k}_{\parallel}^{\mu\prime} - \mathbf{k}_{\parallel}^{v})]\delta(E' - E \mp \hbar\omega_{\mathrm{LO}}), \end{aligned} \tag{26a}$$

$$\langle C_{ab\to ij}^{\mu\to v}\rangle = \int_{C_{ij}} \mathrm{d}E\,\mathrm{d}\theta \int_{C_{ab}} \mathrm{d}E'\,\mathrm{d}\theta' c_2(\mathbf{k}_{\parallel}^{v}, \mathbf{k}_{\parallel}^{\mu\prime})\delta(E - E_i)\lambda_a^{\mathrm{E}}(E')\delta(\theta - \theta_j)\delta(\theta' - \theta_b)\delta(E' - E). \tag{26b}$$

In addition, the phonon collision terms $D_1[r_{xy}]$ and $D_2[r_{xy}]$ are given by

$$\mathscr{D}_1[r_{xy}] = \sum_{v,\mu}\sum_{i=1}^{N}\sum_{j=1}^{M}\sum_{a=1}^{N}\sum_{b=1}^{M} n_{ij}^{v}[1_{ab}^{\mu} - n_{ab}^{\mu}]\{\langle S_{ij\to ab,xy}^{v\to\mu}\rangle^{-}[r_{xy} + 1_{xy}^{\mathrm{p}}] - \langle S_{ij\to ab,xy}^{v\to\mu}\rangle^{+} r_{xy}\}, \tag{27}$$

$$\mathscr{D}_2[r_{xy}] = \frac{1}{\tau_{\mathrm{LO}}}[1_{xy}^{\mathrm{p}} g_{\mathrm{BE}} - r_{xy}]. \tag{28}$$

For computing the screening parameter for polar optical and piezoelectric scattering, it is necessary to determine the electron distribution functions at the bottoms of the subbands. These quantities $f^{v}(0)$ are approximated via

$$f^{v}(0) = \sum_{j=1}^{M} \frac{n_{I_{\min}^{v},j}^{v}}{1_{I_{\min}^{v},j}^{v}}, \tag{29}$$

where $I_{\min}^{v}$ is the energy index so that $\varepsilon_v \in [E_{I_{\min}^{v}-1/2}, E_{I_{\min}^{v}+1/2}]$.

5. Numerical results

The simulations shown in this section are performed for the lattice temperature $T_L = 300$ K and the sheet electron density $n = 5 \times 10^{12}$ cm^{-2} by taking into account the four lowest energy subbands. Concerning the parameters used in our numerical scheme, we set $N = 60$, $M = 24$, $n_{mul} = 10$. This implies that $E_{max} = 0.55$ eV. Additionally, we use $R = 50$ and $S = 24$ with the maximum wave vector $q_{max} = 3.6 \times 10^9$ m^{-1}. Initial data for the coefficients n_{ij}^{v} and r_{xy} are obtained by integrating the Fermi–Dirac distribution and the Bose–Einstein distribution over the cells C_{ij} and D_{xy}, respectively. The stationary state is assumed to be reached approximately at 10 ps after the onset of the electric field. All of the required constants are found in Table 1.

5.1. Confining potential

We solve the coupled system of the effective mass Schrödinger and the Poisson equations self-consistently for computing the confining potential and the energy subband structures needed for our transport equations. Therefore, we proceed as follows [3]. In a 2DEG confined in a quantum well at a heterojunction, the electrons move in the potential

$$V(z) = -e\Psi(z) + \Delta E_c \Theta(z - z_0). \tag{30}$$

Here, e is the elementary charge, $\Psi(z)$ denotes the electrostatic potential depending on the position z normal to the AlGaN/GaN interface at $z_0 = 0$ nm (cp. Fig. 1). The symbol ΔE_c labels the interface barrier. The electrostatic potential is related to the charge distribution by the Poisson equation

Table 1
Material parameter for the 2DEG simulation

Quantity	Symbol	Unit	GaN	$Al_{0.15}Ga_{0.85}N$
Electron effective mass[a]	m^*		0.22 m_e	
Static dielectric constant[a]	κ_{st}		8.9	
HF dielectric constant[b]	κ_{hf}		5.23	
Lattice constants[c]	a	nm	0.3189	0.3177
	c	nm	5.185	
Acoustic deformation potential[b]	D_A	eV	8.3	
Longitudinal sound velocity[b]	v_l	m s^{-1}	6560	
Transverse sound velocity[b]	v_t	m s^{-1}	2680	
Mass density[b]	ρ	kg m^{-3}	6150	
Longitudinal optical phonon energy[b]	$\hbar\omega_{LO}$	meV	91.2	
Transverse optical phonon energy[d]	$\hbar\omega_{TO}$	meV	69.5	
Piezoelectric constants[c]	e_{31}	C m^{-2}	−0.49	−0.506
	e_{33}	C m^{-2}	0.73	0.839
	e_{15}	C m^{-2}	−0.3	
Spontaneous polarization[c]	P_{sp}	C m^{-2}	−0.029	−0.0368
Elastic constants[c]	c_{13}	GPa	103.0	103.75
	c_{33}	GPa	405.0	400.2
Averaged elastic constants[e]	c_{LA}	GPa	265	
	c_{TA}	GPa	44.2	
Phonon relaxation time[f]	τ_{LO}	ps	1	
Interface barrier[f]	ΔE_c	eV	0.6	

[a] Ref. [14].
[b] Ref. [15].
[c] Ref. [16].
[d] Ref. [11].
[e] Ref. [17].
[f] Ref. [2].

$$\frac{\mathrm{d}}{\mathrm{d}z}\left[\kappa_{\mathrm{st}}(z)\frac{\mathrm{d}}{\mathrm{d}z}\right]\Psi(z) = -\frac{e}{\kappa_0}[N_{\mathrm{f}}(z) - n(z)], \tag{31}$$

where κ_{st} is the static dielectric constant, κ_0 is the permittivity of free space, $N_{\mathrm{f}}(z)$ stands for the space dependent fixed charge given by the structure of the heterojunction, and $n(z)$ denotes the charge distribution of the quantum confined electrons. This quantity can be evaluated via

$$n(z) = \sum_v \frac{m^*(z)k_{\mathrm{B}}T_{\mathrm{L}}}{\pi\hbar^2}\ln\left[1 + \exp\left(\frac{E_{\mathrm{f}} - \varepsilon_v}{k_{\mathrm{B}}T_{\mathrm{L}}}\right)\right]|\varphi_v(z)|^2, \tag{32}$$

with the lattice temperature T_{L} and the Fermi energy E_{f} for parabolic energy subbands (1) and Fermi statistics taking into account degeneracy effects of the electron gas. The charge of the two-dimensional confined electrons depends on the subband envelope functions and the eigenenergies. These quantities are the solutions of the one-dimensional effective mass Schrödinger equation

$$\left\{-\frac{\hbar^2}{2}\frac{\mathrm{d}}{\mathrm{d}z}\left[\frac{1}{m^*(z)}\frac{\mathrm{d}}{\mathrm{d}z}\right] + V(z)\right\}\varphi_v(z) = \varepsilon_v\varphi_v(z). \tag{33}$$

We apply an iteration procedure to solve (31) and (33). To begin with, we insert a trial 2DEG charge distribution $n(z)$ into the Poisson equation (31). This leads to a confining potential $V(z)$ via (30), which is used in the Schrödinger equation (33) to determine eigenenergies and wave functions. The 2DEG density is corrected with the help of these quantities according to (32). All these calculations are performed by using standard numerical methods. Subsequent iterations lead to the final self-consistent solution for $V(z)$, ε_v and φ_v with the required accuracy.

As shown in [16], spontaneous and piezoelectric polarization play an important role in the quantum-confinement of electrons at AlGaN/GaN interfaces. Hence, we take into account the polarization charge

$$\sigma = P_{\mathrm{sp}}(0.15) - P_{\mathrm{sp}}(0) + 2\frac{a(0) - a(0.15)}{a(0.15)}\left[e_{31}(z) - e_{33}(z)\frac{C_{13}(0.15)}{C_{33}(0.15)}\right] \tag{34}$$

for the fixed charge N_{f} in (31). In the considered configuration, σ is positive and free electrons tend to compensate for it. Following [2], we use a value for the interface band offset ΔE_{c} twice as high as found in the literature [16]. This prevents electrons from entering the AlGaN layer considerably, and we can neglect electron sharing effects. This assumption is justified at not too high electric fields.

Fig. 2 displays the resulting self-consistent solution for the confining potential $V(z)$ and the first four eigenenergies and envelope wave functions, which are used in our transport simulations. Moreover, this figure shows the self-consistent solution for the 2DEG density. The scattering probabilities in our transport model are calculated for these equilibrium self-consistent wave functions. For saving computational time, no field-induced modulations on the ε_v and φ_v are taken into account. Electron scattering into higher valleys is neglected, hence we deal with a spherical and parabolic one-valley many-subband model. These assumptions are valid for the range of electric field strengths under consideration.

5.2. Macroscopic quantities

In Fig. 3, we show the results for the electron velocity-field characteristics at an $Al_xGa_{1-x}N$/GaN heterojunction at 300 K, simulated by means of our multigroup equations. Three cases are considered: including the degeneracy of the 2DEG but neglecting hot phonon effects, neglecting the degeneracy of the electron gas and taking into account hot phonon effects, and including both the degeneracy of the 2DEG and hot phonons into the transport model. The simulations show that the electron gas degeneracy as well as the hot phonon effects influence the electron drift velocity in the investigated range of the electric field. Hence, both

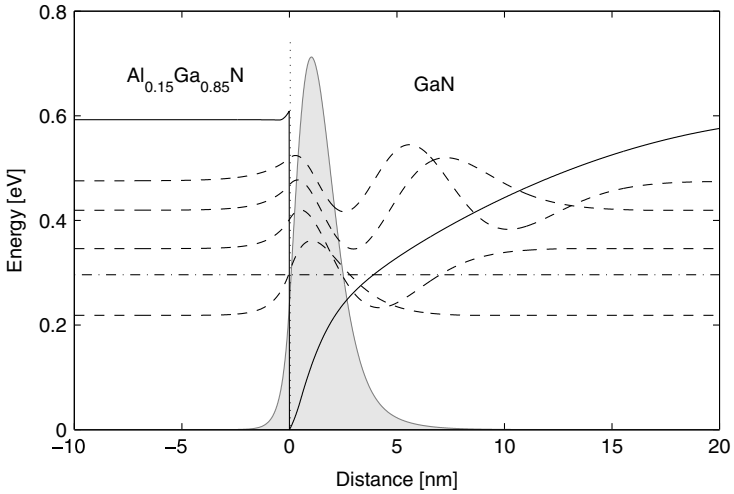

Fig. 2. The potential profile (solid line), the first four wave functions (dashed lines) and the profile of the 2DEG density (filled) versus position. Wave functions and electron density are plotted in arbitrary units; the zero of each wave function is the corresponding eigenenergy. The dashed-dotted line refers to the Fermi energy.

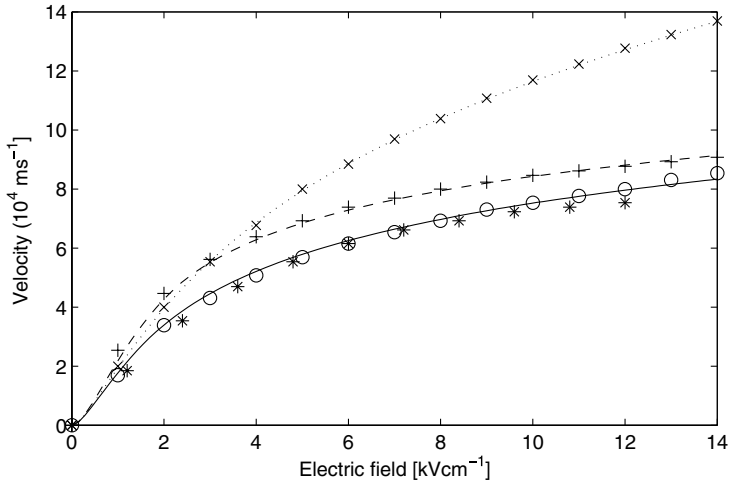

Fig. 3. The electron velocity-field characteristics for the $Al_xGa_{1-x}N/GaN$ heterojunction at 300 K. Lines refer to results from the multigroup method and symbols to MC calculations [2]. (···, ×): degenerated gas, equilibrium phonons; (−−−, +): non-degenerated gas, hot phonons; (—, ○): degenerated gas, hot phonons; ∗: experiment [18].

effects must be taken into account for good agreement with experimental data [18]. Moreover, we observe excellent agreement of our results with those of MC calculations [2].

When degeneracy is neglected, the drift velocity exceeds that obtained by the full model. This can be explained in terms of the angular dependence of the final electron states after phonon emission. Small angle scattering by phonon emission processes is the dominant scattering mechanism for electrons with wave vectors in direction of the drift velocity, if the degeneracy is neglected. When the Pauli principle is applied, this small angle scattering rate reduces dramatically, since the corresponding final states are occupied. Consequently, the probability for large angle scattering is enhanced, and electrons are forced to scatter to final

states in opposite direction of the drift velocity. This implies a strong negative contribution to the drift velocity. Since the mean electron energy increases as the electric field increases, electron gas degeneracy effects decrease with the rising electric field. Hence, the drift velocity curves calculated with and without degeneracy tend to merge at high fields [2].

When the hot phonon effects are not taken into account, the calculated drift velocity exceeds considerably the experimental data and the results of the simulation for the complete model. Hence, hot phonon effects can be regarded as quite important in nitride heterostructures. Due to the enhanced phonon occupation number (cp. Fig. 10), hot phonons support a stronger scattering of electrons. The scattering caused by the optical phonon absorption increases because of the phonon reabsorption; the scattering caused by phonon emission increases due to the stimulated emission. This explains the essential reduction in the drift velocity when hot phonons are taken into account. The stronger the electric field, the more pronounced are the hot phonon effects [2].

Finally, we note a deviation of the calculated drift velocity from the experimental data in Fig. 3 for fields higher than 10 kV cm^{-1}. It is known that electron sharing influences the experimental results on the drift velocity at stronger electric fields [18]. The sharing of electrons by the $Al_xGa_{1-x}N$ and the GaN layer has not been taken into account in this simulation, which leads to the higher calculated drift velocity in comparison to the experimentally determined one for high fields.

In Figs. 4–6, we depict the temporal evolution of the densities, the velocities and the mean energies of electrons confined at an $Al_xGa_{1-x}N$/GaN heterojunction for the three lowest subbands in response to the onset of an electric field pulse of the strength $\mathscr{E} = 10$ kV cm^{-1}. Solid lines refer to calculations taking into account hot phonons; the dashed curves are obtained by assuming equilibrium phonons. In both simulations, degeneracy of the 2DEG is regarded. For times $t < 0.2$ ps, the results of the two considered cases almost agree, while the increasing phonon density (cp. Fig. 10) leads to significant differences in the macroscopic quantities for later times in correspondence with the stationary state values displayed in Fig. 3.

The most interesting result of these simulations is the behavior of the drift velocity with time. We observe a velocity overshoot as it is expected for the relatively high electric field. In the case of the equilibrium phonon calculation, this velocity overshoot is caused by the ballistic transport of electrons right after the onset of the electric field, when the distribution function is shifted by the electric field but hardly altered

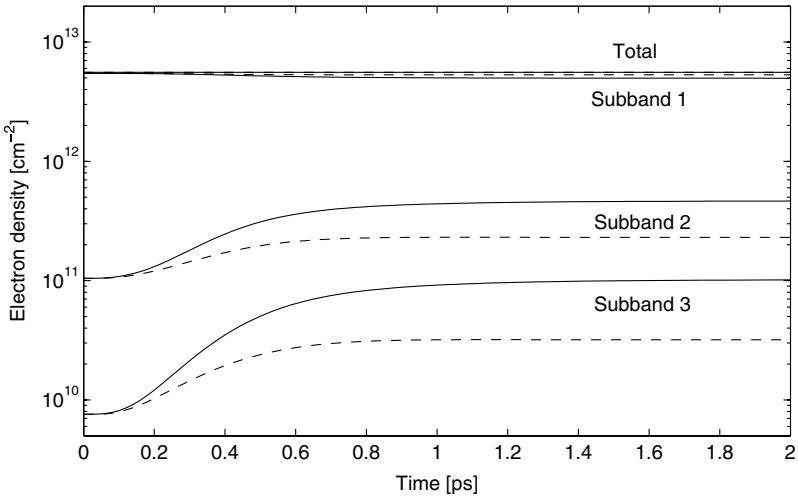

Fig. 4. Temporal evolution of the electron densities in the three lowest subbands of a 2DEG formed at an AlGaN/GaN heterojunction after the onset of the electric field with $|\mathbf{E}_\parallel| = 10$ kV cm^{-1}. Solid lines: hot phonons; dashed lines: equilibrium phonons.

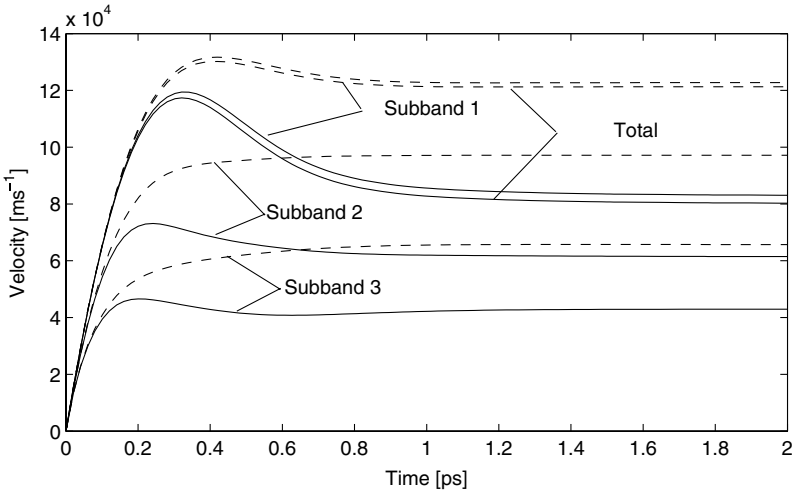

Fig. 5. Temporal evolution of the drift velocities in the three lowest subbands of a 2DEG formed at an AlGaN/GaN heterojunction after the onset of the electric field with $|\mathbf{E}_{\|}| = 10\ \mathrm{kV\ cm^{-1}}$. Solid lines: hot phonons; dashed lines: equilibrium phonons.

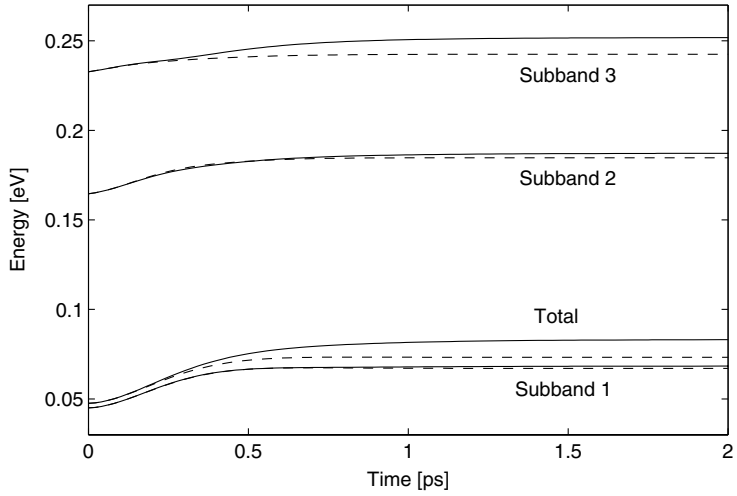

Fig. 6. Temporal evolution of the mean energies in the three lowest subbands of a 2DEG formed at an AlGaN/GaN heterojunction after the onset of the electric field with $|\mathbf{E}_{\|}| = 10\ \mathrm{kV\ cm^{-1}}$. Solid lines: hot phonons; dashed lines: equilibrium phonons.

by scattering events. This ballistic motion contributes to the velocity overshoot in the hot phonon simulation as well; however, the dominant reason for the decrease of the velocity with increasing time is the enhanced phonon scattering caused by the non-equilibrium phonons. Their effect is strong enough to cause a velocity overshoot, not only in the lowest subband as it is the case in the equilibrium phonon simulation, but also for the higher ones. Moreover, we note that the maximum velocity achieved is much lower in the case of taking into account non-equilibrium phonons. Hence, simulations aimed at designing GaN-based heterostructure semiconductor devices, which take advantage of velocity overshoots for reducing switching times, must include hot phonon effects for not overestimating the achievable performance of such devices.

5.3. Distribution functions

One of the advantages of handling the Bloch–Boltzmann–Peierls equations with the help of deterministic solution methods is the availability of the particle distribution functions in noise-free resolution. Moreover, the consideration of two-dimensional transport problems allows the illustration of the whole information on the distribution function without an averaging procedure. Hence, we regard the following figures as quite illustrative.

Figs. 7–10 depict the stationary-state electron distribution functions for the three lowest energy bands and the associated longitudinal optical phonon distribution function at the $Al_xGa_{1-x}N/GaN$ heterojunc-

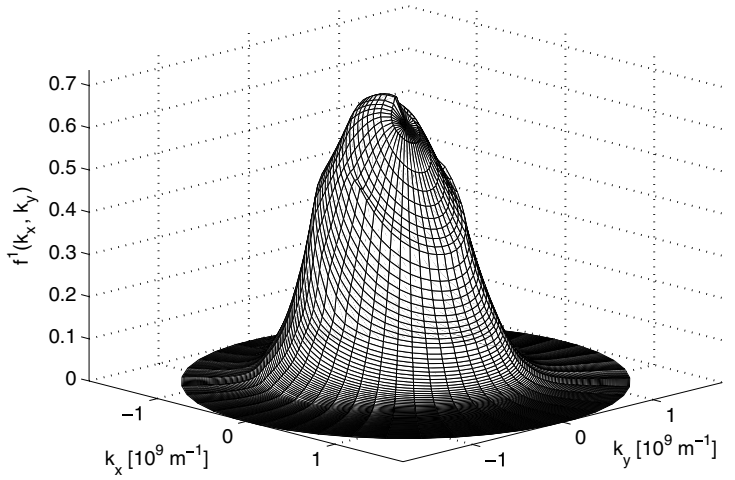

Fig. 7. Stationary-state electron distribution function in the first subband f^1 versus the wave vector $\mathbf{k}_\parallel$ at an AlGaN/GaN heterojunction under the influence of the electric field $|\mathbf{E}_\parallel| = 10\ \mathrm{kV\ cm^{-1}}$.

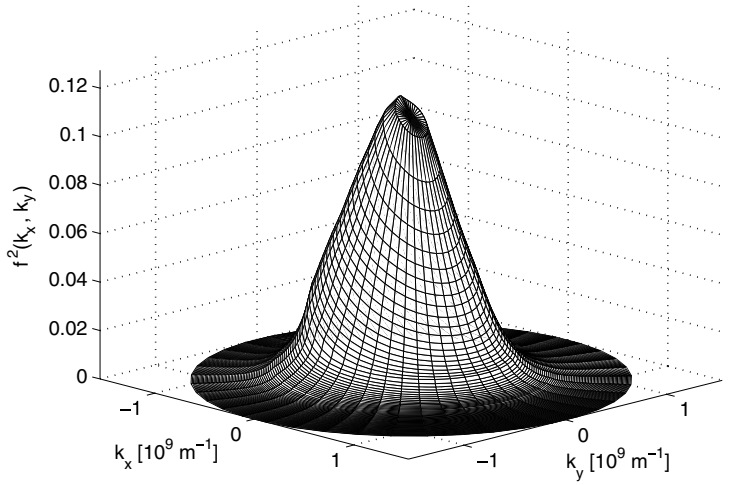

Fig. 8. Stationary-state electron distribution function in the second subband f^2 versus the wave vector $\mathbf{k}_\parallel$ at an AlGaN/GaN heterojunction under the influence of the electric field $|\mathbf{E}_\parallel| = 10\ \mathrm{kV\ cm^{-1}}$.

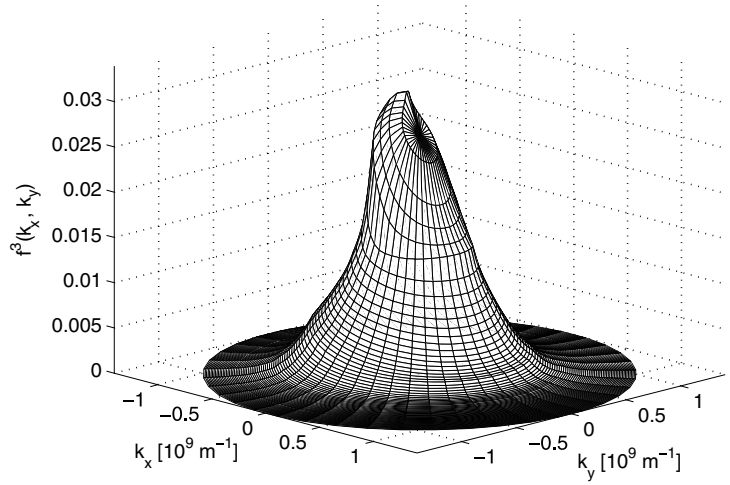

Fig. 9. Stationary-state electron distribution function in the third subband f^3 versus the wave vector $\mathbf{k}_\parallel$ at an AlGaN/GaN heterojunction under the influence of the electric field $|\mathbf{E}_\parallel| = 10\ \mathrm{kV\ cm^{-1}}$.

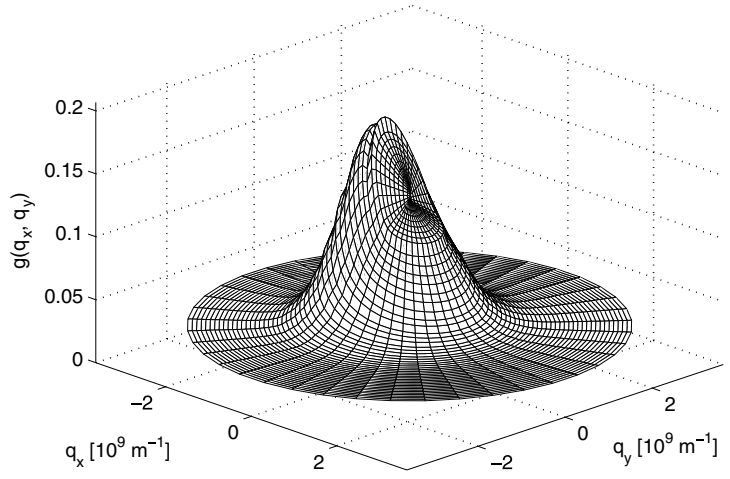

Fig. 10. Stationary-state longitudinal optical phonon distribution function g versus the wave vector $\mathbf{q}_\parallel$ at an AlGaN/GaN heterojunction under the influence of the electric field $|\mathbf{E}_\parallel| = 10\ \mathrm{kV\ cm^{-1}}$.

tion. In this simulation, the electric field is set to $\mathscr{E} = 10\ \mathrm{kV\ cm^{-1}}$. The distribution functions f^{ν}_{ij} and g_{xy} in the points $\mathbf{k}^{\nu}_{ij} = k^{\nu}_{\parallel}(E_i)(\cos\theta_j, \sin\theta_j)$ and $\mathbf{q}_{xy} = q_x(\cos\zeta_y, \sin\zeta_y)$ are approximated via $f^{\nu}_{ij} = n^{\nu}_{ij}\Theta(E_i - \varepsilon_\nu)/1^{\nu}_{ij}$ and $g_{xy} = r^{\nu}_{xy}/1^{\mathrm{p}}_{xy}$.

In Figs. 7–9, we observe that the electron distribution functions can be seen as shifted Fermi–Dirac distributions with some abrupt changes in their falling with rising energies. This finer structure is related to the onset of possible intersubband scattering. In contrast to bulk polar semiconductors with their large differences in the effective masses of Γ-valley and L-valley electrons, the density of states is the same for all subbands for 2DEGs. This results in the less pronounced decline in the distribution function of a subband

when starting to overlap with another one in comparison to the bulk case when intervalley scattering begins to take place [5].

In Fig. 10, we see the reason for the strong influence of the hot phonon effect on the electron drift velocity. The phonon distribution function is significantly enhanced in comparison to its equilibrium Bose–Einstein value (equals here the value in the undisturbed regions for large $\mathbf{q}_\parallel$). Another interesting feature of g is its behavior for very small $\mathbf{q}_\parallel$. In bulk semiconductors, there exists a value $q_{\min} > 0$ so that scattering by phonons with $|\mathbf{q}| < q_{\min}$ is prohibited because of the conservation of momentum and energy. In confined systems, $q_{\min}$ tends to zero, since the constant optical phonon energy is converted into potential energy of electrons by intersubband scattering processes. Thus, the phonon distribution function does not exhibit an undisturbed region centered at $\mathbf{q}_\parallel = 0$ in the case of two-dimensional transport but only a small inversion as it is observable in Fig. 10.

6. Conclusion

We present multigroup model equations for directly solving the two-dimensional Bloch–Boltzmann–Peierls equations, which govern the transport of electrons and LO phonons at heterojunctions. With the help of this deterministic approach, we investigate the two-dimensional electron transport in AlGaN/GaN heterostructures in presence of strain polarization fields. The envelope wave functions for the confined electrons are calculated using a self-consistent Poisson–Schrödinger solver. The electron gas degeneracy and hot phonons are included in our transport equations. Numerical results are given for the field and time dependence of macroscopic quantities and for the electron and the phonon distribution functions. The obtained results exhibit good agreement with those of Monte Carlo simulations.

Acknowledgments

This work has been supported by the Fond zur Förderung der wissenschaftlichen Forschung, Vienna, under Contract Number P17438-N08.

References

[1] H. Morkoç, Nitride Semiconductors and Devices, Springer, Heidelberg, 1999.
[2] M. Ramonas, A. Matulionis, L. Rota, Monte Carlo simulation of hot-phonon and degeneracy effects in the AlGaN/GaN two-dimensional electron gas channel, Semicond. Sci. Technol. 18 (2003) 118.
[3] D.K. Ferry, S.M. Goodnick, Transport in Nanostructures, Cambridge University Press, Cambridge, 1997.
[4] E.M. Lifschitz, L.P. Pitaevskii, Physical Kinetics, Pergamon Press, Oxford, 1981.
[5] M. Galler, F. Schürrer, A deterministic solution approach for the coupled system of transport equations for the electrons and phonons in polar semiconductors, J. Phys. A. Math. Gen. 37 (2003) 1479.
[6] M. Galler, F. Schürrer, Multigroup equations to the hot-electron hot-phonon system in III–V compound semiconductors, Comput. Methods Appl. Mech. Engrg. 194 (2005) 2806.
[7] J.M. Ziman, Electrons and Phonons, Clarendon Press, Oxford, 2001.
[8] J. Kolnik, I.H. Oguzman, K.F. Brennan, R. Wang, P.P. Ruden, Y. Wang, Electronic transport studies of bulk zincblende and wurtzite phases of GaN based on an ensemble Monte Carlo calculation including a full zone bandstructure, J. Appl. Phys. 78 (1995) 1033.
[9] A.R. Hutson, Piezoelectric scattering and phonon drag in ZnO and CdS, J. Appl. Phys. 32 (1961) 2287.
[10] S.M. Goodnick, P. Lugli, Influence of electron-hole scattering on subpicosecond carrier relaxation in $Al_xGa_{1-x}As$/GaAs quantum wells, Phys. Rev. B 38 (1988) 10135.
[11] C. Bulutay, B.K. Ridley, N.A. Zakhleniuk, Full band polar optical phonon scattering analysis and negative differential conductivity in wurtzite GaN, Phys. Rev. B 62 (2000) 15754.

[12] P.J. Price, Two-dimensional electron transport in semiconductor layers. I. Phonon scattering, Ann. Phys. 133 (1981) 217.
[13] R.J. LeVeque, Numerical Methods for Conservation Laws, Birkhäuser, Basel, 1992.
[14] R. Gaska, J.W. Yang, A. Osinsky, Q. Chen, M.A. Khan, A.O. Orlov, G.L. Snider, M.S. Shur, Electron transport in AlGaN–GaN heterostructures grown on 6H–SiC substrates, Appl. Phys. Lett. 72 (1998) 707.
[15] S.K. O'Leary, B.E. Foutz, M.S. Shur, U.V. Bhapkar, L.F. Eastman, Electron transport in wurtzite indium nitride, J. Appl. Phys. 83 (1998) 826.
[16] O. Ambacher, J. Smart, J.R. Shealy, N.G. Weimann, K. Chu, M. Murphy, R. Dimitrov, L. Wittmer, M. Stutzmann, W. Rieger, J. Hilsenbeck, Two-dimensional electron gases induced by spontaneous and piezoelectric polarization in N- and Ga-face AlGaN/GaN heterostructures, J. Appl. Phys. 85 (1999) 3222.
[17] B.K. Ridley, B.E. Foutz, L.F. Eastman, Mobility of electrons in bulk GaN and $Al_xGa_{1-x}N$/GaN heterostructures, Phys. Rev. B 61 (2000) 16862.
[18] A. Matulionis, J. Liberis, L. Ardaravičus, M. Ramonas, T. Zubkutė, I. Matulionienė, F. Eastman, J.R. Shealy, J. Smart, Fast and ultrafast processes in AlGaN/GaN channels, Phys. Stat. Sol. b 234 (2002) 826.